










# Suspended germanium waveguides with subwavelength-grating metamaterial cladding for the mid-infrared band

ALEJANDRO SÁNCHEZ-POSTIGO,<sup>1,\*</sup>  ALEJANDRO ORTEGA-MOÑUX,<sup>1</sup> JORDI SOLER PENADÉS,<sup>2,3</sup> AHMED OSMAN,<sup>2</sup>  MILOŠ NEDELJKOVIĆ,<sup>2</sup>  ZHIBO QU,<sup>2</sup> YANGBO WU,<sup>2</sup>  ÍÑIGO MOLINA-FERNÁNDEZ,<sup>1</sup>  PAVEL CHEBEN,<sup>4</sup>  GORAN Z. MASHANOVICH,<sup>2</sup> AND J. GONZALO WANGÜEMERT-PÉREZ<sup>1</sup> 

<sup>1</sup>Universidad de Málaga, Dpto. Ingeniería de Comunicaciones, ETSI Telecomunicación, 29071 Málaga, Spain

<sup>2</sup>Optoelectronics Research Centre, University of Southampton, Southampton, SO17 1BJ, United Kingdom

<sup>3</sup>Currently at VLC Photonics S.L., Valencia, Spain

<sup>4</sup>National Research Council Canada, 1200 Montreal Road, Bldg. M50, Ottawa K1A 0R6, Canada

\*asp@ic.uma.es

**Abstract:** In recent years, sensing and communication applications have fueled important developments of group-IV photonics in the mid-infrared band. In the long-wave range, most platforms are based on germanium, which is transparent up to  $\sim 15\text{-}\mu\text{m}$  wavelength. However, those platforms are limited by the intrinsic losses of complementary materials or require complex fabrication processes. To overcome these limitations, we propose suspended germanium waveguides with a subwavelength metamaterial lateral cladding that simultaneously provides optical confinement and allows structural suspension. These all-germanium waveguides can be fabricated in one dry and one wet etch step. A propagation loss of 5.3 dB/cm is measured at a wavelength of 7.7  $\mu\text{m}$ . These results open the door for the development of integrated devices that can be fabricated in a simple manner and can potentially cover the mid-infrared band up to  $\sim 15\text{ }\mu\text{m}$ .

Published by The Optical Society under the terms of the [Creative Commons Attribution 4.0 License](https://creativecommons.org/licenses/by/4.0/). Further distribution of this work must maintain attribution to the author(s) and the published article's title, journal citation, and DOI.

## 1. Introduction

The mid-infrared (MIR) band (wavelengths from  $\lambda \sim 2\text{ }\mu\text{m}$  to  $\lambda \sim 20\text{ }\mu\text{m}$ ) has been attracting increasing attention from researchers in group-IV photonics, particularly because of the promising opportunities that this wavelength range offers for optical communications [1], sensing [2], and on-chip spectroscopy [3]. Extending the operation range of waveguide sensors [4–9] and on-chip spectrometers [10–16] typically designed for near-IR to MIR is of significant interest, as molecules of many gases and liquids present characteristic vibrational absorption peaks that can be exploited for detection of biological and chemical species. Low-loss group-IV photonics components are required for the development of cost-effective, ultra-compact lab-on-chip devices [17].

The silicon-on-insulator (SOI) platform is of limited relevance for the MIR band. The intrinsic losses of silicon dioxide and silicon become prohibitive above wavelengths of  $\sim 4\text{ }\mu\text{m}$  and  $\sim 8\text{ }\mu\text{m}$ , respectively, thus limiting SOI utilization in the long-wave range [18]. To overcome this problem, materials other than silicon and silicon dioxide can be used [19,20], leading to waveguide platforms such as silicon on sapphire [21], silicon on silicon nitride [22], germanium on silicon [23,24], germanium on SOI [25], or silicon-germanium-based platforms [26–28]. Alternatively,

the silicon dioxide layer can be partially or fully removed to create pedestals or suspended membranes, primarily limited by the material loss of the guiding layer [29–36].

We have demonstrated suspended silicon waveguides with subwavelength-grating (SWG) metamaterial lateral cladding [32]. Unlike other silicon membranes that are based on rib waveguides [31], our platform can be easily fabricated, using one dry and one wet etch step. Propagation losses as low as 0.8 dB/cm and 3.1 dB/cm were achieved at wavelengths of 3.8  $\mu\text{m}$  and 7.7  $\mu\text{m}$ , respectively. The comparatively high loss at 7.7- $\mu\text{m}$  wavelength is attributed to the silicon material loss. Germanium is transparent up to about 15  $\mu\text{m}$  and is therefore an excellent choice for suspended platforms at long wavelengths.

In this work, we present the first experimental demonstration of a suspended germanium waveguide with SWG lateral cladding. SWG metamaterials, since their early demonstration in silicon waveguides [37–43], have been advantageously used to manipulate light in integrated photonic devices [44,45]. The proposed germanium waveguides enable light propagation at longer wavelengths compared to silicon waveguides and also provide interesting optical properties such as higher refractive index contrast and optical nonlinearity [46]. From a fabrication point of view, our platform is simpler than state-of-the-art suspended germanium alternatives [35,36]. Furthermore, the top and bottom air cladding facilitates the interaction of light with the analyte molecules, thereby increasing the sensitivity to effective index changes, which is an obvious advantage for sensing applications compared to other platforms, including Ge-on-Si or SiGe [24,27]. As a proof of concept, we performed our experiments at a wavelength of 7.7  $\mu\text{m}$ , demonstrating propagation losses of  $5.3 \pm 1.0$  dB/cm.

This article is organized as follows: In Section 2, a suspended germanium waveguide is investigated and designed. In Section 3, the fabrication process of suspended waveguides is presented. The experimental characterization is shown in Section 4. A discussion about the suitability of the suspended germanium platform at longer wavelengths is provided in Section 5. Finally, conclusions are drawn in Section 6.

## 2. Waveguide modeling and design

### 2.1. Waveguide geometry

A waveguide schematic in Ge-on-SOI platform is illustrated in Fig. 1. The core, of width  $W_{\text{wg}}$  and thickness  $H_{\text{wg}}$ , is anchored to lateral unetched germanium regions by a periodically patterned cladding membrane of pitch  $\Lambda$ . The cladding, of width  $W_{\text{clad}}$ , comprises strips and holes of lengths  $L_{\text{Ge}}$  and  $L_{\text{air}}$ , respectively. An air gap of thickness  $H_{\text{air}} \sim H_{\text{BOX}} = 3$   $\mu\text{m}$  separates the guiding layer from the silicon substrate.

### 2.2. Design constraints

To ensure single-mode operation with low propagation loss, suspended waveguides are designed taking into account the following considerations:

- (i) *Mechanical stability.* The SWG cladding must be mechanically robust and the torque must be low enough to prevent structural collapse and breaks in the cladding strips.
- (ii) *Fabrication requirements.* The cladding holes must be sufficiently large to allow the flow of the HF etching solution to remove the bottom cladding. Remnants of silicon dioxide can dramatically increase the propagation loss. Besides, the fabrication process imposes a minimum feature size, which depends on the thickness of the Ge guiding layer.
- (iii) *Optical properties.* First, to avoid Bragg reflections, the period of the cladding must satisfy the subwavelength-grating condition ( $\Lambda < 0.5\lambda n_{\text{B}}$ , where  $n_{\text{B}}$  is the effective index of the fundamental Bloch–Floquet mode). Second, to enable practical single-mode operation,

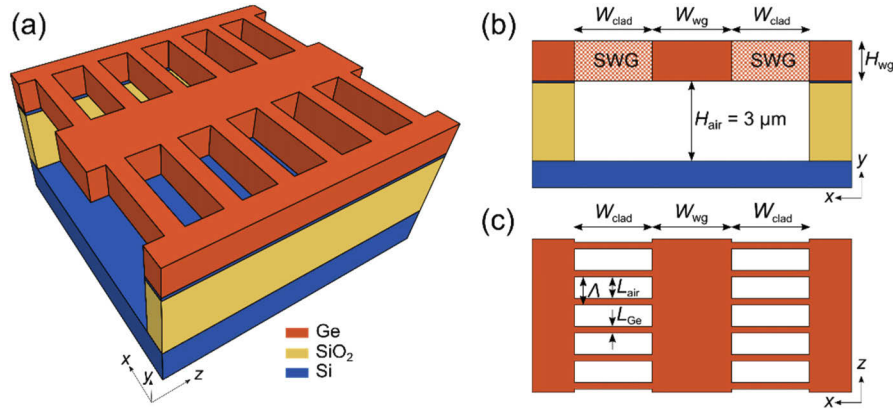


**Fig. 1.** Schematics of a suspended germanium waveguide with subwavelength-grating metamaterial lateral cladding. (a) 3D view. (b) Front view, with the lateral cladding being replaced by a homogeneous SWG metamaterial. (c) Top view of the guiding layer.

the fundamental mode must propagate with negligible vertical [47] and lateral leakage losses, and high-order modes, if guided, must be leaky.

To satisfy these considerations simultaneously requires a trade-off between the geometrical parameters of the waveguide. For example, a thick germanium layer is needed to reduce the vertical leakage for the fundamental mode, but a thin, lightweight waveguide can favor single-mode operation and can facilitate the flow of the liquid acid solution. A comprehensive analysis of the influence of the geometrical parameters of suspended waveguides on the fulfilment of these requirements can be found in [32].

### 2.3. Design of suspended germanium waveguides

The ultimate design goal is to minimize the propagation loss ( $\alpha$ ) of the fundamental mode supported by the suspended waveguide while maintaining single-mode operation and ensuring mechanical stability. In our design flow, we assume that the loss is primarily limited by the power leakage to the silicon substrate ( $\alpha_{\text{vertical}}$ ) and the lateral germanium slab ( $\alpha_{\text{lateral}}$ ).

Since our suspended waveguide is a periodic structure, it supports guided modes as Bloch–Floquet solutions of Maxwell’s equations. The propagation loss is determined by the imaginary part of the effective index of the mode and depends on the geometry of the waveguide. The calculation of Bloch–Floquet modes is rather tedious for state-of-the-art mode solvers [48,49]. To circumvent this limitation, periodic media at subwavelength scale can be modeled as an equivalent homogeneous anisotropic metamaterial that behaves as a uniaxial crystal [50]. The permittivity tensor that describes such an equivalent material,  $\epsilon_{\text{SWG}}$ , is defined as

$$\epsilon_{\text{SWG}} = \begin{pmatrix} n_{xx}^2 & 0 & 0 \\ 0 & n_{xx}^2 & 0 \\ 0 & 0 & n_{zz}^2 \end{pmatrix}. \quad (1)$$

Operating far enough from the Bragg regime ( $\Lambda \ll \lambda$ ), the refractive indices  $n_{xx}$  and  $n_{zz}$  can be approximated by Rytov’s formulas [51]:

$$n_{xx} \sim [\text{DC} \cdot n_{\text{Ge}}^2 + (1 - \text{DC}) \cdot n_{\text{air}}^2]^{1/2}, \quad (2)$$

$$n_{zz} \sim [\text{DC} \cdot n_{\text{Ge}}^{-2} + (1 - \text{DC}) \cdot n_{\text{air}}^{-2}]^{-1/2}, \quad (3)$$

where  $n_{\text{Ge}}$  is the refractive index of the germanium strips,  $n_{\text{air}}$  is the refractive index of the air holes, and DC is the duty cycle of the lateral cladding ( $\text{DC} = L_{\text{Ge}}/\Lambda$ ). We utilize the finite-difference mode solver in Photon Design's FIMMWAVE [52], which supports anisotropic materials, to simulate suspended waveguides with a homogenized metamaterial lateral cladding, as defined in Eq. (1). Compared to the isotropic approach used in our previous works [32,53–55], the anisotropic model provides more accurate results without increasing the simulation time. More advantageously, these results are achieved at a fraction of the computational cost that would be required if a full-vectorial Bloch–Floquet analysis were performed.

For the nominal wavelength of  $7.7 \mu\text{m}$ , our mode calculations show that the vertical leakage for the fundamental mode is negligible ( $\alpha_{\text{vertical}} < 0.1 \text{ dB/cm}$ ) for germanium layers that are thicker than  $0.8 \mu\text{m}$ . This low loss is due to the strong modal confinement that is caused by the high Ge-air index contrast. We chose  $H_{\text{wg}} = 1 \mu\text{m}$  because of wafer availability in our laboratory. For this thickness, the vertical second-order mode ( $\text{TE}_{01}$ ) is cut off. Furthermore, small over-etching during the fabrication process would still ensure vertical single-mode operation (see Section 3 for further information on fabrication).

The waveguide core width ( $W_{\text{wg}}$ ) and the SWG cladding geometry ( $W_{\text{clad}}$ ,  $L_{\text{Ge}}$ , and  $L_{\text{air}}$ ) are chosen to meet fabrication and mechanical requirements while ensuring that the lateral leakage is negligible for the fundamental mode and is high for the horizontal second-order mode ( $\text{TE}_{01}$ ), should the latter be supported by the structure. As a starting point, we scaled the width of a standard photonic wire at a wavelength of  $1.55 \mu\text{m}$  ( $W_{\text{wg}} = 0.5 \mu\text{m}$ ), obtaining a starting width  $W_{\text{wg}} \sim 2.5 \mu\text{m}$ . According to our previous experiments [32,54,55], to guarantee the integrity of the waveguides the lateral cladding width  $W_{\text{clad}}$  should be smaller than  $4 \mu\text{m}$  and the length  $L_{\text{Ge}}$  of the lateral strips should be at least  $200 \text{ nm}$ . On the other hand, as we experimentally found, holes smaller than  $400 \text{ nm}$  may hinder the HF flow, which constitutes a lower bound for  $L_{\text{air}}$ . Taking into account these constraints, by simulation we have determined a set of geometrical parameters that provide both good optical performance and robust mechanical behavior (see Table 1). For this waveguide geometry, Fig. 2 shows the simulated electric field distributions of the fundamental mode, which is strongly guided, and the second-order mode, substantially delocalized from the waveguide core with a leakage loss exceeding  $80 \text{ dB/cm}$ .

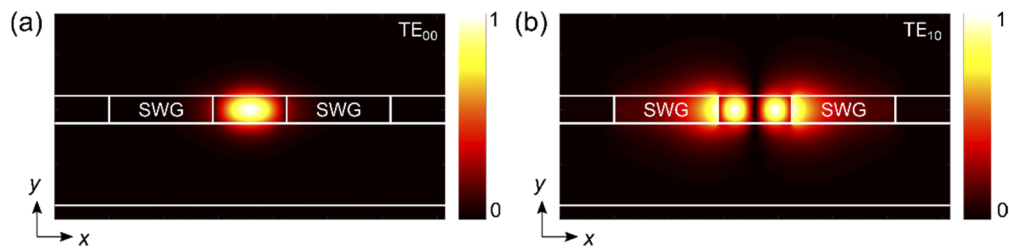


**Fig. 2.** Simulated electric field ( $E_x$  component) of the (a) fundamental mode and (b) second-order mode supported by the suspended Ge waveguide, with the nominal dimensions as in Table 1. The fundamental mode is well confined within the waveguide core, which ensures negligible leakage. The second-order mode expands laterally, with the evanescent field reaching the lateral germanium slab, yielding a high lateral leakage enabling effective single-mode operation.

**Table 1. Nominal Dimensions of the Designed Suspended Germanium Waveguide ( $\lambda = 7.7 \mu\text{m}$ )**

$H_{\text{wg}}$ ( $\mu\text{m}$ )	$H_{\text{air}}$ ( $\mu\text{m}$ )	$W_{\text{wg}}$ ( $\mu\text{m}$ )	$W_{\text{clad}}$ ( $\mu\text{m}$ )	$L_{\text{Ge}}$ ( $\mu\text{m}$ )	$L_{\text{air}}$ ( $\mu\text{m}$ )
1.0	3.0	2.7	3.8	0.2	0.8

### 3. Fabrication

Our suspended germanium waveguides are implemented in Ge-on-SOI wafers. The fabrication of these wafers starts with standard SOI substrates [silicon thickness: 220 nm, buried oxide (BOX) thickness:  $H_{\text{BOX}} = 3 \mu\text{m}$ ], which are then thermal oxidized and wet etched to thin the Si layer to about 50–60 nm. Then, the Ge guiding layer is grown by reduced pressure chemical vapor deposition (RPCVD).

A ZEP520-A photosensitive resist was spun onto the germanium layer of the sample and the suspended waveguides were defined by e-beam lithography. An inductively coupled plasma (ICP) process with  $\text{SF}_6\text{-C}_4\text{F}_8$  chemistry was used to etch the germanium areas that were not protected by the photoresist (the holes of the suspended structures). Using an ellipsometer, we estimated the etch rate and checked the etch depth at several stages of the dry etch process. We etched the germanium layer and the thin silicon film, thus exposing the buried silicon dioxide, as required for the membrane structural suspension [see Fig. 3(a)].

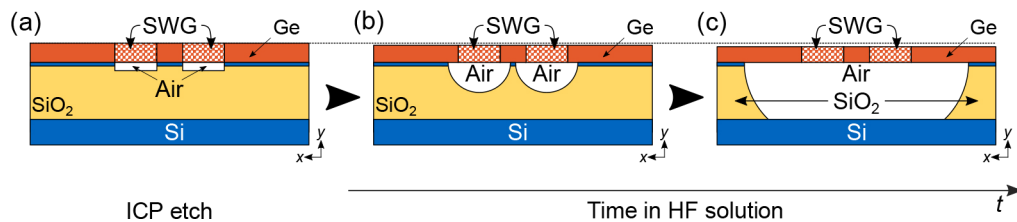


**Fig. 3.** Fabrication procedure of suspended germanium waveguides with subwavelength-grating lateral cladding. (a) The cladding holes are transferred from the photoresist to the germanium layer and thin silicon film underneath by dry (ICP) etching, thus exposing the buried silicon dioxide. (b) The sample is dipped into an HF acid solution, which starts wet etching the silicon dioxide and the remaining silicon film. (c) After sufficient submerging time, the thin silicon film and the buried oxide are fully removed.

Once the dry etch step was finished, the sample was dipped into a 1:7 HF:H<sub>2</sub>O solution to remove the buried oxide, the remaining photoresist, and the un-etched remnants of the thin silicon film that were underneath the un-etched germanium. The wet etch time calibration is critical. Under-etching would leave residual silicon dioxide [see Fig. 3(b)], hence increasing propagation loss, while too long exposure to HF can reduce the thickness and widths of germanium structures. To compensate for the over-etching in both the dry and the wet etch processes, device flavors with increased parameters  $W$ ,  $W_{\text{clad}}$ , and  $L_{\text{Ge}}$  were fabricated. We left the samples for  $\sim 2$  hours in the HF tank to remove the thin silicon film and the silicon dioxide under the widest structures (tapers and input/output fiber-chip couplers) [see Fig. 3(c)].

Several sets of waveguides were fabricated in a sample, with an effective area of  $3 \text{ mm} \times 2 \text{ mm}$ , to measure the propagation loss using the cut-back method, as will be discussed in Section 4. The waveguides in each set had a variation in the width of the features of 50 nm with respect to the waveguides in the adjacent set. The main goal of the variations was to study fabrication biases and to guarantee structural suspension and mechanical stability.

Figure 4 shows a focused-ion-beam (FIB) scanning-electron-microscope (SEM) image of one of the fabricated suspended germanium waveguides. The thin silicon film and the buried silicon dioxide under the germanium guiding layer are fully removed and the structure remains stable, with no apparent bending nor breaks in the germanium strips. We measured an over-etching in the widths of the features of  $\sim 150$  nm, while a reduction of less than 55 nm was observed in the germanium thickness. According to our simulations, the influence of the latter in the leakage loss is negligible.



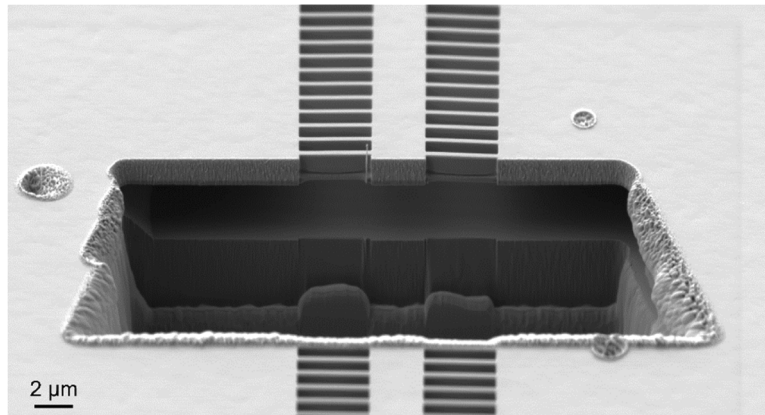


**Fig. 4.** Focused-ion-beam (FIB) cut of one of the fabricated suspended germanium waveguides. The structure is fully suspended and stable, with no apparent breaks or bending.

## 4. Experimental characterization

### 4.1. Measurement setup

The characterization of the suspended waveguides was performed using our MIR grating-coupling measurement setup, schematically shown in Fig. 5. Light is injected to the chip from a continuous-wave distributed-feedback quantum cascade laser. A black diamond-2 lens with a focal length of 1.9 mm is used as a collimator. To improve the signal-to-noise ratio, the light beam is modulated by a chopper wheel with a frequency of 300–400 Hz. A set of mirrors is used to direct the light toward the input optical fiber (IRFlex IRF-Se-12 [56]) via a focusing black diamond-2 lens with 5.95-mm focal distance. Due to the relatively small mode field diameter of the optical fiber (13.6  $\mu\text{m}$  at a wavelength of 7.7  $\mu\text{m}$ ), the light is coupled into the chip via an ultra-broadband suspended germanium micro-antenna [57]. The light is extracted from the chip using a micro-antenna to the output optical fiber, carrying the light toward a HgCdTe detector. The signal is detected by using a lock-in amplifier.

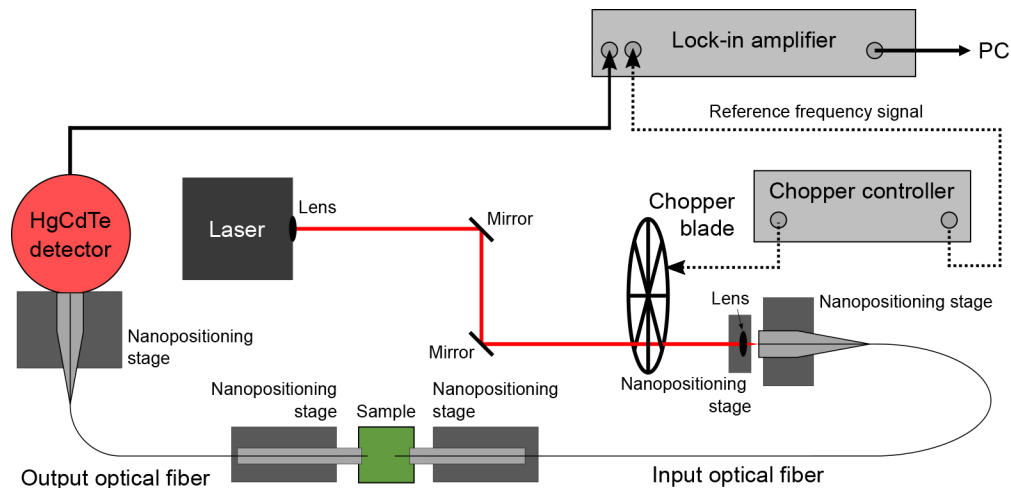


**Fig. 5.** Schematic representation of the measurement setup used to characterize suspended germanium waveguides at 7.7- $\mu\text{m}$  wavelength.

## 4.2. Experimental results

Suspended germanium waveguides were characterized by measuring the transmitted power through waveguides of different lengths, using the cut-back method [58]. This method filters out uncertainties in the transmitted power, provided that the alignment of the setup is maintained during the measurement process. Propagation losses before HF etching were high ( $>60$  dB/cm), but could not be calculated accurately because the measured power was below the noise floor of our photodetector. After removing the BOX, a propagation loss of 5.2 dB/cm was measured for the waveguide in the SEM image [see Fig. 6(a)]. In this SEM image, we observe a change in the duty cycle from 20% to 25%, while the other dimensions are in excellent agreement with the nominal design. By simulation, we estimate a leakage loss of  $\sim 0.5$  dB/cm for the dimensions of the measured structure. We attribute the rest of the loss to the following sources: (i) surface and sidewall roughness; (ii) threading dislocations at the Ge-Si interface between the Ge layer and the thin Si layer of the original Ge-on-SOI wafer [35]; and (iii) contamination on the surfaces of the SOI wafers before growth of the germanium layer (between 1,500 and 12,500 contamination sites per 6" wafer observed in the wafer batch by optical metrology before the growth process), expected to result in defect filled Ge material above the contamination sites.

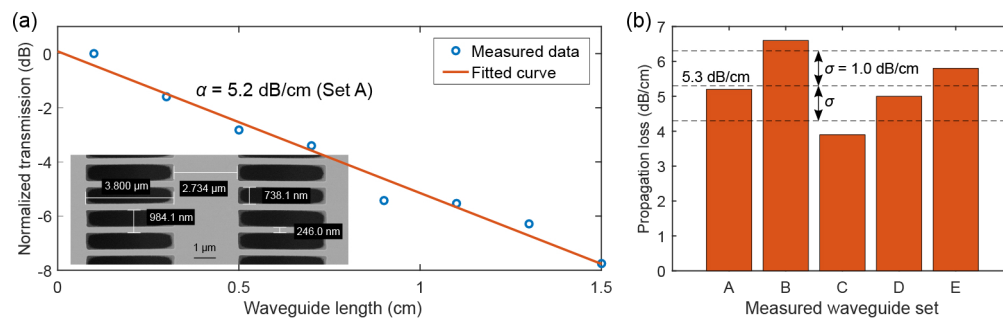


**Fig. 6.** (a) Transmitted optical power as a function of the waveguide length (normalized to the measured power at the output of the shortest waveguide), with a best fit line to estimate the propagation loss. The SEM image shows the actual dimensions of the waveguide. (b) Measured propagation loss of several waveguide sets with minimal geometrical variations, showing an average propagation loss of  $5.3 \pm 1.0$  dB/cm. The waveguide measured in Fig. 6(a) corresponds to set A.

Finally, to study the reproducibility of the waveguides, we calculated the propagation loss of five sets of waveguides, as shown in Fig. 6(b). Waveguides within a given set have the same geometry, while waveguides of different sets have variations in the dimensions. Those variations, however, are minimal and of limited relevance for the leakage loss, so that the propagation losses of the waveguides of different sets can be compared. A mean propagation loss of 5.3 dB/cm is obtained, with a standard deviation of 1.0 dB/cm.

## 5. Discussion

Our experiments demonstrate the appropriateness of the suspended germanium platform for mid-infrared applications at a wavelength of 7.7  $\mu\text{m}$ , with a propagation loss of  $5.3 \pm 1.0$  dB/cm. In this section, we discuss the suitability of the platform at 15- $\mu\text{m}$  wavelength, the upper bound of the transparency region of germanium.

To guarantee low-loss propagation at long wavelengths, the waveguide cross-section ( $H_{\text{wg}} = 1$   $\mu\text{m}$ ,  $W_{\text{wg}} = 2.7$   $\mu\text{m}$ , and  $W_{\text{clad}} = 3.8$   $\mu\text{m}$  at 7.7- $\mu\text{m}$  wavelength) must be redesigned. There are several options to maintain single-mode operation with negligible leakage: to increase the core thickness  $H_{\text{wg}}$  or the air-gap thickness  $H_{\text{air}}$ . The simulated propagation loss ( $\alpha$ ) of a suspended germanium

waveguide as a function of the air-gap thickness is analyzed at 15- $\mu\text{m}$  wavelength in Fig. 7(a), for core thicknesses of 1  $\mu\text{m}$ , 2  $\mu\text{m}$ , and 3  $\mu\text{m}$ , and assuming no material loss in the Ge guiding layer. The core width is scaled up by a factor of  $\sim 2$  ( $W_{\text{wg}} = 5.5 \mu\text{m}$ ) and the cladding width is considered infinite to prevent lateral leakage. The same lateral index contrast as in our demonstrated waveguide at 7.7- $\mu\text{m}$  wavelength is kept. From this analysis, the thickness optimization options that are needed at 15- $\mu\text{m}$  wavelength are as follows:

- (1) When a thickness  $H_{\text{wg}}$  of 1  $\mu\text{m}$  is used, as at 7.7- $\mu\text{m}$  wavelength, a leakage loss exceeding 150 dB/cm is obtained for the fundamental mode when  $H_{\text{air}} = H_{\text{BOX}} = 3 \mu\text{m}$ . This high loss can be reduced by increasing  $H_{\text{air}}$  up to  $\sim 7.5 \mu\text{m}$  ( $H_{\text{air}} = H_{\text{BOX}} + \sim 4.5 \mu\text{m}$ ), which can be achieved by dipping the sample in a 25% aqueous tetramethylammonium hydroxide (TMAH) bath after the first (HF) wet etch process. Assuming the same anisotropic silicon etch rate of 7.3 nm/min as reported in [35], the required air-gap thickness can be reached after  $\sim 10$  hours, with negligible ( $\sim 4.5$  nm) reduction in the thickness of the germanium layer.
- (2) A thickness  $H_{\text{wg}}$  of 2  $\mu\text{m}$ , corresponding to the scaled-up version of the waveguide at 7.7- $\mu\text{m}$  wavelength, would require  $H_{\text{air}} = 4.75 \mu\text{m}$  ( $H_{\text{BOX}} + 1.75 \mu\text{m}$ ), which can be achieved after a 4-hour TMAH immersion.
- (3) To attain a propagation loss of only 0.1 dB/cm without increasing the thickness  $H_{\text{air}}$  (i.e., maintaining  $H_{\text{air}} = H_{\text{BOX}} = 3 \mu\text{m}$ ), a thickness  $H_{\text{wg}}$  of  $\sim 3 \mu\text{m}$  is required. In this case, the  $\text{TE}_{01}$  mode (second-order vertical mode) exhibits a propagation loss in excess of 50 dB/cm even for a slab waveguide.

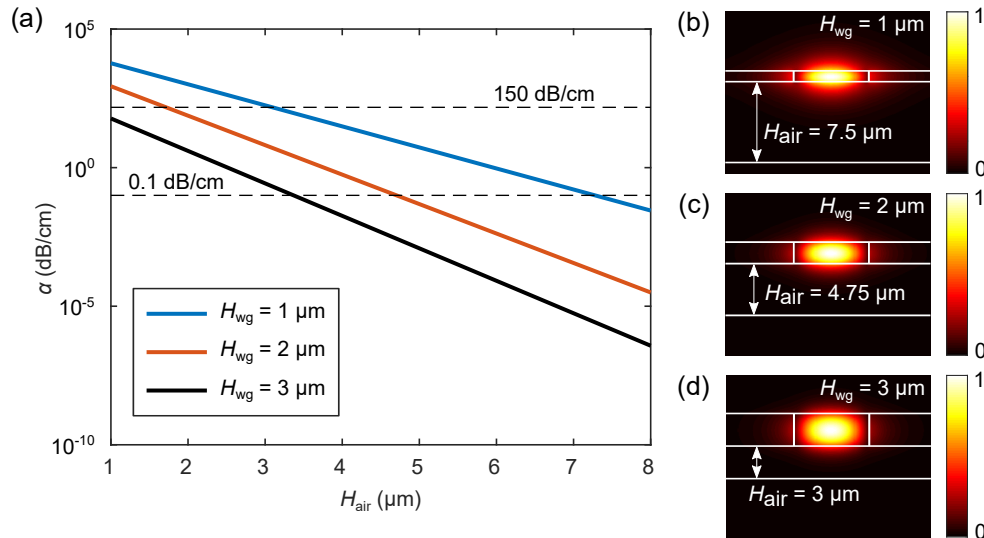


**Fig. 7.** (a) Propagation loss as a function of the air-gap thickness for several guiding-layer thicknesses at a wavelength of 15  $\mu\text{m}$ . The width of the waveguide core is scaled up to 5.5  $\mu\text{m}$  to laterally confine the fundamental mode, while the width of the subwavelength-grating cladding is considered infinite to avoid lateral leakage. The same lateral index contrast as in the nominal design at 7.7- $\mu\text{m}$  wavelength is maintained. (b, c, d) Simulated electric field ( $E_x$  component) of the fundamental mode supported by a suspended germanium waveguide of (b)  $H_{\text{wg}} = 1 \mu\text{m}$ , (c)  $H_{\text{wg}} = 2 \mu\text{m}$ , and (d)  $H_{\text{wg}} = 3 \mu\text{m}$ .

Once the loss due to the silicon substrate is avoided using the structural modifications in (1)–(3), the lateral dimensions must be chosen in order to ensure mechanical stability, fabrication



feasibility, and low lateral leakage for the fundamental mode. For the thicknesses in (1)–(3), Fig. 7(b), 7(c), and 7(d) show the simulated electric field of the fundamental mode ( $E_x$  component). As expected, the thinner the waveguide core, the more laterally delocalized the mode field, thus requiring wider waveguide core or lateral cladding to achieve low lateral leakage. Table 2 summarizes the design dimensions of several suspended germanium waveguides. The core widths have been chosen to ensure low-loss propagation ( $\sim 1$  dB/cm) using robust, narrow claddings ( $W_{\text{clad}} \leq 4 \mu\text{m}$ ). Alternative cladding widths are suggested for negligible lateral leakage ( $\sim 0.1$  dB/cm), but the robustness of such waveguides should be experimentally confirmed. Note that, for thicker guiding layers, greater cladding widths can likely be used without jeopardizing stability. In the proposed designs, to facilitate the flow of the etching solutions, we have increased the length of the holes with the germanium thickness while keeping the period ( $\Lambda = L_{\text{Ge}} + L_{\text{air}}$ ) below the Bragg threshold ( $\Lambda_{\text{Bragg}} \sim 2.2 \mu\text{m}$ ). These results confirm theoretically that the proposed suspended germanium platform can be used not only at 7.7- $\mu\text{m}$  wavelength, but also at longer mid-infrared wavelengths, provided that the waveguides are conveniently designed.

**Table 2. Nominal Dimensions of the Designed Suspended Germanium Waveguides ( $\lambda = 15.0 \mu\text{m}$ )**

$H_{\text{wg}}$ ( $\mu\text{m}$ )	$H_{\text{air}}$ ( $\mu\text{m}$ )	$W_{\text{wg}}$ ( $\mu\text{m}$ )	$W_{\text{clad}}$ ( $\mu\text{m}$ ) @ $\alpha_{\text{lateral}} \sim 1$ dB/cm	$W_{\text{clad}}$ ( $\mu\text{m}$ ) @ $\alpha_{\text{lateral}} \sim 0.1$ dB/cm	$L_{\text{Ge}}$ ( $\mu\text{m}$ )	$L_{\text{air}}$ ( $\mu\text{m}$ )
1.0	7.50	9.0	4.0	6.0	0.25	0.75
2.0	4.75	6.5	3.9	5.6	0.35	1.10
3.0	3.00	5.5	3.0	5.0	0.50	1.50

## 6. Conclusions

While silicon waveguides can only operate up to a wavelength of  $\sim 8 \mu\text{m}$  because of their intrinsic material loss, the transparency range of germanium, up to a wavelength of  $15 \mu\text{m}$ , makes this material an excellent choice for the long-wave infrared band. Suspended germanium waveguides are particularly interesting as they can potentially provide low-loss propagation up to  $15\text{-}\mu\text{m}$  wavelength. In this work, we have reported for the first time a suspended germanium waveguide with subwavelength-grating metamaterial lateral cladding at a mid-infrared wavelength of  $7.7 \mu\text{m}$ , with a propagation loss of  $5.3 \pm 1.0$  dB/cm. The inherent anisotropic nature of SWG metamaterials has been considered in the design procedure to avoid undesired leakage losses. Compared to state-of-the-art suspended germanium alternatives, our platform has a simpler fabrication process, using one dry and one wet etch step. Our SWG-engineered germanium waveguide platform opens promising prospects for development of planar waveguide devices for the applications in the mid-infrared band, at wavelengths from  $2 \mu\text{m}$  to  $15 \mu\text{m}$ .

**Funding.** Ministerio de Ciencia, Innovación y Universidades (PID2019-106747RB-I00); Consejería de Economía, Conocimiento, Empresas y Universidad, Junta de Andalucía (P18-RT-1453, P18-RT-793, UMA18-FEDERJA-219); Universidad de Málaga; Engineering and Physical Sciences Research Council (EP/N00762X/1).

**Disclosures.** The authors declare that there are no conflicts of interest related to this article.

## References

1. V. Vakarín, J. Ramírez, J. Frigerio, Q. Liu, A. Ballabio, X. Le Roux, C. Alonso-Ramos, G. Isella, P. Cheben, W. N. Ye, L. Vivien, and D. Marris-Morini, "Wideband Ge-rich SiGe polarization-insensitive waveguides for mid-infrared free-space communications," *Appl. Sci.* **8**(7), 1154 (2018).
2. Q. Liu, J. M. Ramirez, V. Vakarín, X. Le Roux, A. Ballabio, J. Frigerio, D. Chrastina, G. Isella, D. Bouville, L. Vivien, C. A. Ramos, and D. Marris-Morini, "Mid-infrared sensing between 5.2 and 6.6  $\mu\text{m}$  wavelengths using Ge-rich SiGe waveguides [Invited]," *Opt. Mater. Express* **8**(5), 1305–1312 (2018).
3. M. Nedeljkovic, A. V. Velasco, A. Z. Khokhar, A. Delage, P. Cheben, and G. Z. Mashanovich, "Mid-infrared silicon-on-insulator Fourier-transform spectrometer chip," *IEEE Photonics Technol. Lett.* **28**(4), 528–531 (2016).
4. S. Janz, D.-X. Xu, M. Vachon, N. Sabourin, P. Cheben, H. McIntosh, H. Ding, S. Wang, J. H. Schmid, A. Delage, J. Lapointe, A. Densmore, R. Ma, W. Sinclair, S. M. Logan, R. MacKenzie, Q. Y. Liu, D. Zhang, G. Lopinski, O.

- Mozenon, M. Gilmour, and H. Tabor, "Photonic wire biosensor microarray chip and instrumentation with application to serotyping of *Escherichia coli* isolates," *Opt. Express* **21**(4), 4623–4637 (2013).
5. J. Gonzalo Wangüemert-Pérez, P. Cheben, A. Ortega-Moñux, C. Alonso-Ramos, D. Pérez-Galacho, R. Halir, I. Molina-Fernández, D.-X. Xu, and J. H. Schmid, "Evanescent field waveguide sensing with subwavelength grating structures in silicon-on-insulator," *Opt. Lett.* **39**(15), 4442–4445 (2014).
  6. J. G. Wangüemert-Pérez, A. Hadji-Elhouati, A. Sánchez-Postigo, J. Leuermann, D.-X. Xu, P. Cheben, A. Ortega-Moñux, R. Halir, and Í. Molina-Fernández, "[INVITED] Subwavelength structures for silicon photonics biosensing," *Opt. Laser Technol.* **109**, 437–448 (2019).
  7. A. Densmore, E. Post, D.-X. Xu, P. Waldron, S. Janz, P. Cheben, J. Lapointe, A. Delage, B. Lamontagne, and J. H. Schmid, "A silicon-on-insulator photonic wire based evanescent field sensor," *IEEE Photonics Technol. Lett.* **18**(23), 2520–2522 (2006).
  8. F. Dell'Olivo and V. M. Passaro, "Optical sensing by optimized silicon slot waveguides," *Opt. Express* **15**(8), 4977–4993 (2007).
  9. L. Tombez, E. J. Zhang, J. S. Orcutt, S. Kamapurkar, and W. M. J. Green, "Methane absorption spectroscopy on a silicon photonic chip," *Optica* **4**(11), 1322–1325 (2017).
  10. P. Cheben, "Wavelength Dispersive Planar Waveguide Devices: Echelle and Arrayed Waveguide Gratings," in *Optical Waveguides: From Theory to Applied Technologies*, M. L. Calvo and V. Lakshminarayanan, eds. (CRC Press, 2007), p. 58.
  11. P. J. Bock, P. Cheben, A. V. Velasco, J. H. Schmid, A. Delâge, M. Florjańczyk, J. Lapointe, D.-X. Xu, M. Vachon, S. Janz, and M. L. Calvo, "Subwavelength grating Fourier-transform interferometer array in silicon-on-insulator," *Laser Photonics Rev.* **7**(6), L67–L70 (2013).
  12. P. Cheben, A. L. Bogdanov, A. Delage, S. Janz, B. Lamontagne, M.-J. Picard, E. Post, and D.-X. Xu, "A 100-channel near-infrared SOI waveguide microspectrometer: design and fabrication challenges," in H. Ming, X. Zhang, and M. Y. Chen, eds. (2005), p. 103.
  13. P. Cheben, S. Janz, M. Florjańczyk, and D.-X. Xu, "Planar waveguide wavelength dispersive devices with multiple waveguide input aperture," U.S. patent 8,351,043 (2009).
  14. D. M. Kita, B. Miranda, D. Favela, D. Bono, J. Michon, H. Lin, T. Gu, and J. Hu, "High-performance and scalable on-chip digital Fourier transform spectroscopy," *Nat. Commun.* **9**(1), 4405 (2018).
  15. S. N. Zheng, J. Zou, H. Cai, J. F. Song, L. K. Chin, P. Y. Liu, Z. P. Lin, D. L. Kwong, and A. Q. Liu, "Microring resonator-assisted Fourier transform spectrometer with enhanced resolution and large bandwidth in single chip solution," *Nat. Commun.* **10**(1), 2349 (2019).
  16. H. Wang, Z. Lin, Q. Li, and W. Shi, "On-chip Fourier transform spectrometers by dual-polarized detection," *Opt. Lett.* **44**(11), 2923–2926 (2019).
  17. T. Hu, B. Dong, X. Luo, T.-Y. Liow, J. Song, C. Lee, and G.-Q. Lo, "Silicon photonic platforms for mid-infrared applications [Invited]," *Photonics Res.* **5**(5), 417–430 (2017).
  18. R. Soref, "Mid-infrared photonics in silicon and germanium," *Nat. Photonics* **4**(8), 495–497 (2010).
  19. Y. Zou, S. Chakravarty, C.-J. Chung, X. Xu, and R. T. Chen, "Mid-infrared silicon photonic waveguides and devices [Invited]," *Photonics Res.* **6**(4), 254–276 (2018).
  20. D. Marris-Morini, V. Vakarin, J. M. Ramirez, Q. Liu, A. Ballabio, J. Frigerio, M. Montesinos, C. Alonso-Ramos, X. Le Roux, S. Serna, D. Benedikovic, D. Chrastina, L. Vivien, and G. Isella, "Germanium-based integrated photonics from near- to mid-infrared applications," *Nanophotonics* **7**(11), 1781–1793 (2018).
  21. T. Baehr-Jones, A. Spott, R. Ilic, A. Spott, B. Penkov, W. Asher, and M. Hochberg, "Silicon-on-sapphire integrated waveguides for the mid-infrared," *Opt. Express* **18**(12), 12127–12135 (2010).
  22. S. Khan, J. Chiles, J. Ma, and S. Fathpour, "Silicon-on-nitride waveguides for mid- and near-infrared integrated photonics," *Appl. Phys. Lett.* **102**(12), 121104 (2013).
  23. G. Z. Mashanovich, F. Y. Gardes, D. J. Thomson, Y. Hu, K. Li, M. Nedeljkovic, J. Soler Penades, A. Z. Khokhar, C. J. Mitchell, S. Stankovic, R. Topley, S. A. Reynolds, Y. Wang, B. Troia, V. M. N. Passaro, C. G. Littlejohns, T. Dominguez Bucio, P. R. Wilson, and G. T. Reed, "Silicon photonic waveguides and devices for near- and mid-IR applications," *IEEE J. Sel. Top. Quantum Electron.* **21**(4), 407–418 (2015).
  24. K. Gallacher, R. W. Millar, U. Griškevičiūtė, L. Baldassarre, M. Sorel, M. Ortolani, and D. J. Paul, "Low loss Ge-on-Si waveguides operating in the 8–14  $\mu\text{m}$  atmospheric transmission window," *Opt. Express* **26**(20), 25667–25675 (2018).
  25. U. Younis, S. K. Vanga, A. E.-J. Lim, P. G.-Q. Lo, A. A. Bettiol, and K.-W. Ang, "Germanium-on-SOI waveguides for mid-infrared wavelengths," *Opt. Express* **24**(11), 11987–11993 (2016).
  26. J. M. Ramirez, V. Vakarin, C. Gilles, J. Frigerio, A. Ballabio, P. Chaisakul, X. Le Roux, C. Alonso-Ramos, G. Maisons, L. Vivien, M. Carras, G. Isella, and D. Marris-Morini, "Low-loss Ge-rich  $\text{Si}_{0.2}\text{Ge}_{0.8}$  waveguides for mid-infrared photonics," *Opt. Lett.* **42**(1), 105–108 (2017).
  27. J. M. Ramirez, Q. Liu, V. Vakarin, J. Frigerio, A. Ballabio, X. Le Roux, D. Bouville, L. Vivien, G. Isella, and D. Marris-Morini, "Graded SiGe waveguides with broadband low-loss propagation in the mid infrared," *Opt. Express* **26**(2), 870–877 (2018).
  28. J. Frigerio, L. Vivien, J. M. Ramirez, A. Ballabio, V. Vakarin, P. Chaisakul, X. Le Roux, G. Isella, D. Marris-Morini, and D. Chrastina, "Ge-rich graded-index  $\text{Si}_{1-x}\text{Ge}_x$  waveguides with broadband tight mode confinement and flat anomalous dispersion for nonlinear mid-infrared photonics," *Opt. Express* **25**(6), 6561 (2017).

29. P. T. Lin, V. Singh, Y. Cai, L. C. Kimerling, and A. Agarwal, "Air-clad silicon pedestal structures for broadband mid-infrared microphotonic," *Opt. Lett.* **38**(7), 1031–1033 (2013).
30. J. Chiles, S. Khan, J. Ma, and S. Fathpour, "High-contrast, all-silicon waveguiding platform for ultra-broadband mid-infrared photonics," *Appl. Phys. Lett.* **103**(15), 151106 (2013).
31. Z. Cheng, X. Chen, C. Y. Wong, K. Xu, and H. K. Tsang, "Mid-infrared suspended membrane waveguide and ring resonator on silicon-on-insulator," *IEEE Photonics J.* **4**(5), 1510–1519 (2012).
32. A. Sánchez-Postigo, J. G. Wangüemert-Pérez, J. Soler Penadés, A. Ortega-Moñux, M. Nedeljkovic, R. Halir, F. El Mokhtari Mimun, Y. Xu Cheng, Z. Qu, A. Z. Khokhar, A. Osman, W. Cao, C. G. Littlejohns, P. Cheben, G. Z. Mashanovich, and Í. Molina-Fernández, "Mid-infrared suspended waveguide platform and building blocks," *IET Optoelectron.* **13**(2), 55–61 (2019).
33. J. Kang, Z. Cheng, W. Zhou, T.-H. Xiao, K.-L. Gopalakrishna, M. Takenaka, H. K. Tsang, and K. Goda, "Focusing subwavelength grating coupler for mid-infrared suspended membrane germanium waveguides," *Opt. Lett.* **42**(11), 2094–2097 (2017).
34. W. Zhou, Z. Cheng, X. Wu, X. Sun, and H. K. Tsang, "Fully suspended slot waveguide platform," *J. Appl. Phys.* **123**(6), 063103 (2018).
35. A. Osman, M. Nedeljkovic, J. Soler Penades, Y. Wu, Z. Qu, A. Z. Khokhar, K. Debnath, and G. Z. Mashanovich, "Suspended low-loss germanium waveguides for the longwave infrared," *Opt. Lett.* **43**(24), 5997–6000 (2018).
36. T.-H. Xiao, Z. Zhao, W. Zhou, C.-Y. Chang, S. Y. Set, M. Takenaka, H. K. Tsang, Z. Cheng, and K. Goda, "Mid-infrared high-Q germanium microring resonator," *Opt. Lett.* **43**(12), 2885–2888 (2018).
37. P. Cheben, D.-X. Xu, S. Janz, and A. Densmore, "Subwavelength waveguide grating for mode conversion and light coupling in integrated optics," *Opt. Express* **14**(11), 4695–4702 (2006).
38. J. H. Schmid, P. Cheben, S. Janz, J. Lapointe, E. Post, and D.-X. Xu, "Gradient-index antireflective subwavelength structures for planar waveguide facets," *Opt. Lett.* **32**(13), 1794–1796 (2007).
39. J. H. Schmid, P. Cheben, S. Janz, J. Lapointe, E. Post, A. Delâge, A. Densmore, B. Lamontagne, P. Waldron, and D.-X. Xu, "Subwavelength grating structures in silicon-on-insulator waveguides," *Adv. Opt. Technol.* **2008**, 1–8 (2008).
40. P. J. Bock, P. Cheben, J. H. Schmid, A. Delâge, D.-X. Xu, S. Janz, and T. J. Hall, "Sub-wavelength grating mode transformers in silicon slab waveguides," *Opt. Express* **17**(21), 19120–19133 (2009).
41. J. H. Schmid, P. Cheben, P. J. Bock, R. Halir, J. Lapointe, S. Janz, A. Delage, A. Densmore, J.-M. Fedeli, T. J. Hall, B. Lamontagne, R. Ma, I. Molina-Fernandez, and D.-X. Xu, "Refractive index engineering with subwavelength gratings in silicon microphotonic waveguides," *IEEE Photonics J.* **3**(3), 597–607 (2011).
42. P. Cheben, J. H. Schmid, D.-X. Xu, A. Densmore, and S. Janz, "Composite subwavelength-structured waveguide in optical systems," U.S. patent 8,503,839 (2013).
43. P. Cheben, S. Janz, D.-X. Xu, J. H. Schmid, A. Densmore, and J. Lapointe, "Interface device for performing mode transformation in optical waveguides," U.S. patent 7,680,371 (2010).
44. P. Cheben, R. Halir, J. H. Schmid, H. A. Atwater, and D. R. Smith, "Subwavelength integrated photonics," *Nature* **560**(7720), 565–572 (2018).
45. R. Halir, A. Ortega-Moñux, D. Benedikovic, G. Z. Mashanovich, J. G. Wangüemert-Pérez, J. H. Schmid, Í. Molina-Fernández, and P. Cheben, "Subwavelength-grating metamaterial structures for silicon photonic devices," *Proc. IEEE* **106**(12), 2144–2157 (2018).
46. N. K. Hon, R. Soref, and B. Jalali, "The third-order nonlinear optical coefficients of Si, Ge, and  $\text{Si}_{1-x}\text{Ge}_x$  in the midwave and longwave infrared," *J. Appl. Phys.* **110**(1), 011301 (2011).
47. J. D. Sarmiento-Merenguel, A. Ortega-Moñux, J.-M. Fédéli, J. G. Wangüemert-Pérez, C. Alonso-Ramos, E. Durán-Valdeiglesias, P. Cheben, Í. Molina-Fernández, and R. Halir, "Controlling leakage losses in subwavelength grating silicon metamaterial waveguides," *Opt. Lett.* **41**(15), 3443–3446 (2016).
48. A. Taflove and S. C. Hagness, *Computational Electrodynamics* (Artech House, 1998).
49. A. Taflove and S. C. Hagness, "Calculation of band structure," in *Computational Electrodynamics: The Finite-Difference Time-Domain Method*, 3rd ed. (Artech House, 2005), pp. 774–787.
50. R. Halir, P. Cheben, J. M. Luque-González, J. D. Sarmiento-Merenguel, J. H. Schmid, G. Wangüemert-Pérez, D.-X. Xu, S. Wang, A. Ortega-Moñux, and Í. Molina-Fernández, "Ultra-broadband nanophotonic beamsplitter using an anisotropic sub-wavelength metamaterial," *Laser Photonics Rev.* **10**(6), 1039–1046 (2016).
51. S. M. Rytov, "Electromagnetic properties of a finely stratified medium," *Sov. Phys. JETP* **2**, 466–475 (1956).
52. . "Mode Solvers – Waveguide CAD Software – FIMMWAVE," <https://www.photond.com/products/fimmwave.htm>.
53. J. Soler Penadés, C. Alonso-Ramos, A. Z. Khokhar, M. Nedeljkovic, L. A. Boodhoo, A. Ortega-Moñux, I. Molina-Fernández, P. Cheben, and G. Z. Mashanovich, "Suspended SOI waveguide with sub-wavelength grating cladding for mid-infrared," *Opt. Lett.* **39**(19), 5661–5664 (2014).
54. J. Soler Penadés, A. Ortega-Moñux, M. Nedeljkovic, J. G. Wangüemert-Pérez, R. Halir, A. Z. Khokhar, C. Alonso-Ramos, Z. Qu, I. Molina-Fernández, P. Cheben, and G. Z. Mashanovich, "Suspended silicon mid-infrared waveguide devices with subwavelength grating metamaterial cladding," *Opt. Express* **24**(20), 22908–22916 (2016).
55. J. Soler Penadés, A. Sánchez-Postigo, M. Nedeljkovic, A. Ortega-Moñux, J. G. Wangüemert-Pérez, Y. Xu, R. Halir, Z. Qu, A. Z. Khokhar, A. Osman, W. Cao, C. G. Littlejohns, P. Cheben, I. Molina-Fernández, and G. Z. Mashanovich, "Suspended silicon waveguides for long-wave infrared wavelengths," *Opt. Lett.* **43**(4), 795–798 (2018).
56. . "Infrared Fiber Optics | IRFlex Corporation," <https://www.irflex.com/products/irf-se-series/>.

57. A. Sánchez-Postigo, A. Ortega-Moñux, D. Pereira-Martín, Í. Molina-Fernández, R. Halir, P. Cheben, J. Soler Penadés, M. Nedeljkovic, G. Z. Mashanovich, and J. G. Wangüemert-Pérez, “Design of a suspended germanium micro-antenna for efficient fiber-chip coupling in the long-wavelength mid-infrared range,” *Opt. Express* **27**(16), 22302–22315 (2019).
58. Y. A. Vlasov and S. J. McNab, “Losses in single-mode silicon-on-insulator strip waveguides and bends,” *Opt. Express* **12**(8), 1622–1631 (2004).